nature energy

ARTICLES

PUBLISHED: 22 FEBRUARY 2016 | ARTICLE NUMBER: 16010 | DOI: 10.1038/NENERGY.2016.10

Selective deposition and stable encapsulation of lithium through heterogeneous seeded growth

Kai Yan[1], Zhenda Lu[1], Hyun-Wook Lee[1], Feng Xiong[1,2], Po-Chun Hsu[1], Yuzhang Li[1], Jie Zhao[1], Steven Chu[3] and Yi Cui[1,4]*

Lithium metal is an attractive anode material for rechargeable batteries, owing to its high theoretical specific capacity of 3,860 mAh g^{-1}. Despite extensive research efforts, there are still many fundamental challenges in using lithium metal in lithium-ion batteries. Most notably, critical information such as its nucleation and growth behaviour remains elusive. Here we explore the nucleation pattern of lithium on various metal substrates and unravel a substrate-dependent growth phenomenon that enables selective deposition of lithium metal. With the aid of binary phase diagrams, we find that no nucleation barriers are present for metals exhibiting a definite solubility in lithium, whereas appreciable nucleation barriers exist for metals with negligible solubility. We thereafter design a nanocapsule structure for lithium metal anodes consisting of hollow carbon spheres with nanoparticle seeds inside. During deposition, the lithium metal is found to predominantly grow inside the hollow carbon spheres. Such selective deposition and stable encapsulation of lithium metal eliminate dendrite formation and enable improved cycling, even in corrosive alkyl carbonate electrolytes, with 98% coulombic efficiency for more than 300 cycles.

Lithium-based batteries are the dominant power sources for consumer electronics, and are also actively being developed for electric vehicles and grid-scale storage[1–3]. Lithium metal anodes and Li–S and Li–air batteries have recently re-emerged with great research attention because of their higher specific capacity compared to existing Li ion technology[4]. Despite research initiated half a century ago[5–7], the problems of lithium dendrites and uncontrollable interfacial chemical reactivity remain. Recent studies, including solid electrolytes for dendrite suppression[8,9], electrolyte and additive tuning[10,11], nanoscale interface design[12,13] and new techniques for understanding[14,15], have marked their progress.

It is well known that Li metal has the highest specific anode capacity of 3,860 mAh g^{-1}, but the electrochemical cycling of Li metal, with its large volume change and unstable interface, presents challenges that compromise safety and cycle-lifetime. There are several critical issues[16]: conductive Li metal could in principle deposit anywhere with unpredictable shapes; deposition of Li metal tends to be highly dendritic; cracking of the solid-electrolyte-interphase (SEI) layer causes electrochemical hot spots and triggers filamentary growth; the persistent reaction between Li metal and electrolyte irreversibly consumes both of them and, therefore, causes severe capacity decay[17–19]. The latter three issues have been partially addressed recently[9–13,20]. However, spatial control over Li deposition, which can help mitigate the latter three issues, still remains elusive. There is no effective approach to spontaneously regulate Li deposition with control over both position and morphology.

Here we report an experimental discovery that there is an appreciable difference in the Li metal nucleation barrier among different substrates, with some materials showing zero overpotential of nucleation. This discovery suggests an effective solution to regulate—and even to encapsulate—lithium metal. By enabling the encapsulation of lithium metal with carbon nanospheres, the cycling efficiency could be improved to 98% for 300 cycles, which is appreciable in a corrosive alkyl carbonate electrolyte.

Lithium nucleation overpotential on various substrates

We studied a list of 11 elemental substrate materials: Au, Ag, Zn, Mg, Al, Pt, Si, Sn, C, Cu and Ni. This list is representative because some of them (Cu, Ni) do not react with Li at room temperature and others form an alloy phase with Li. Cu foil is a common current collector for battery anodes and is also often used for the study of Li metal deposition[12,13]. We here use Cu as a baseline substrate for comparison. Other material substrates were prepared by vacuum deposition with 50 nm of the corresponding thin film onto Cu foil. We then construct a three-electrode electrochemical cell: substrate of interest as working electrode, partly charged $Li_{0.5}FePO_4$ (+3.43 V versus Li/Li$^+$, ~50% state of charge) as the reference electrode and Li metal as the counter electrode. $Li_{0.5}FePO_4$ is a good reference owing to its very stable potential and clear surface nearly free of solid electrolyte interphase[21]. Li metal was galvanostatically deposited on the working electrode at a very small current density (10 μA cm^{-2}) to minimize the overpotential caused by mass transport. For convenience, all the voltage data are presented versus Li metal (Li/Li$^+$) instead of $Li_{0.5}FePO_4$.

Figure 1a shows a voltage profile of Li metal deposition onto bare Cu foil with the oxide removed. There is a significant voltage dip (red dashed circle) at the beginning of Li metal deposition, followed by a flat voltage plateau. The Li metal nucleation overpotential is defined as the difference between the bottom of the voltage dip and the flat part of the voltage plateau. For Cu, the overpotential is ~40 mV, which is used to overcome the heterogeneous nucleation barrier due to the large thermodynamic mismatch between Li and Cu. In contrast, the case for Li metal deposition on Au is very different (Fig. 1b). After two lithiation plateaux to form two alloy phases of Li_xAu above 0 V, the Li metal deposition potential does not show a

[1]Department of Materials Science and Engineering, Stanford University, Stanford, California 94305, USA. [2]Department of Electrical Engineering, Stanford University, Stanford, California 94305, USA. [3]Department of Physics, Stanford University, Stanford, California 94305, USA. [4]Stanford Institute for Materials and Energy Sciences, SLAC National Accelerator Laboratory, 2575 Sand Hill Road, Menlo Park, California 94025, USA.
*e-mail: yicui@stanford.edu

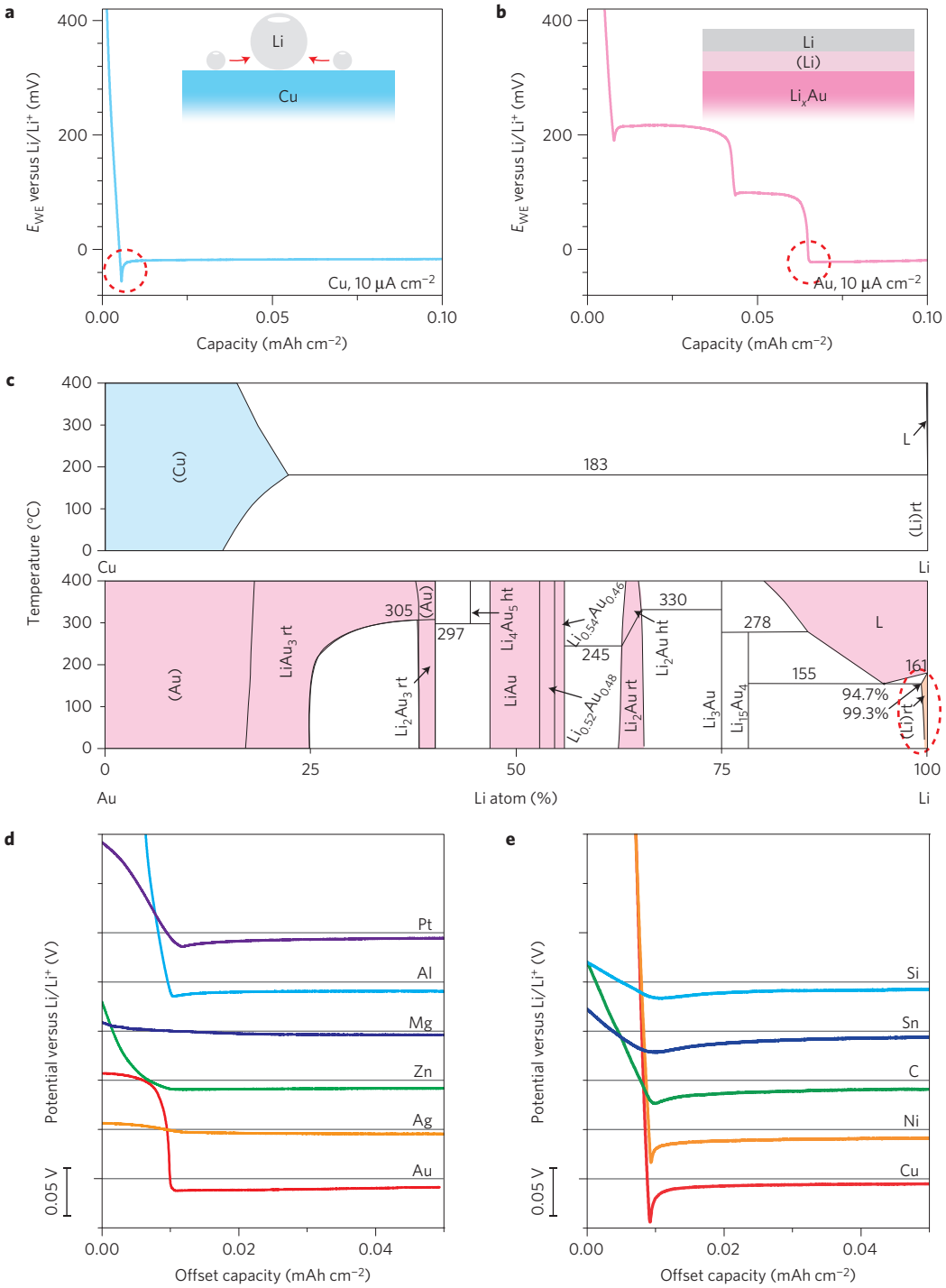

Figure 1 | Overpotential during Li deposition on various substrates. a, Voltage profiles of galvanostatic Li deposition on a copper substrate at 10 μA cm^{-2}. E_{WE} refers to the potential of the working electrode. A clear overpotential was observed, as circled by the dashed line. The inset shows a schematic mechanism of Li nucleation, which explains the extra energy involved. **b**, Voltage profiles of galvanostatic Li deposition on a gold substrate at 10 μA cm^{-2}. As indicated by the dashed circle, no overpotential was observed at the onset of Li metal plating. The inset shows a schematic of how the solid solution buffer layer of Au dissolved in Li reduces the nucleation energy. **c**, Phase diagrams of Li with Cu (up) and Au (bottom). The region where Au dissolved in Li is circled by the dashed line. L refers to liquid, whereas (Li)rt means lithium metal phase at room temperature. **d**, Voltage profiles of various materials with some solubility in Li during Li deposition at a current density of 10 μA cm^{-2}. To enhance the comparison, the curves are shifted horizontally according to the onset of lithium nucleation and vertically with a constant shift of 0.05 V. The scale of the *y*-axis is indicated by the bar in the bottom left. **e**, Shifted voltage profiles of various materials with negligible solubility in Li during Li deposition at a current density of 10 μA cm^{-2}. The horizontal grey lines show 0 V versus Li in **d** and **e**.

dip, but only a sharp right-angle turn at the onset (red dashed circle in Fig. 1b). The Li metal nucleation overpotential on lithiated Au is essentially zero.

To understand the difference between Au and Cu for Li metal nucleation, it is necessary to look at fundamental properties of the heterogeneous nucleation of a material on another solid surface. A

critical parameter for this study is the interfacial energy between substrate and Li metal. The interfacial energy increases with crystal structure mismatch between the two solid phases. Both Au and Cu structures are face-centred cubic whereas Li is body-centred cubic. In addition, their atomic radii are fairly different: Au (1.44 Å), Cu (1.28 Å) and Li (1.52 Å). From this analysis, both Au and Cu should have had energy barriers for Li nucleation. However, if one looks at the binary phase diagram between Li and substrate materials (Fig. 1c), Au not only reacts with Li to form multiple Li_xAu alloy phases, but also has a solubility zone of Au inside Li metal when the atomic ratio of Li is near 100%, giving a solubility of ~0.7 at.% Au in Li at 155 °C and a non-zero value at room temperature. This feature allows the surface gold to dissolve into Li before actual formation of the pure Li phase. With the identical crystal structures of pure Li metal (βLi), this solid solution surface layer can serve as a buffer layer for the subsequent Li deposition, effectively eliminating nucleation barriers. Comparatively, such a solid solution feature does not exist in the case of Cu.

To confirm the hypothesis, we carried out the same experiment on other materials with definite solubility in Li according to the phase diagrams (see Supplementary Fig. 1 for phase diagrams), including Ag (~9 at.%@145.5 °C), Zn (~0.5 at.%@65 °C), Mg (~68 at.%@100 °C), Al (<0.1 at.%@177 °C) and Pt (<0.1 at.%@169 °C). Even though the room temperature solubility data of these materials are not directly available from the phase diagrams, it is reasonable to extrapolate that there would still be some solubility at room temperature. As shown in Fig. 1d, Au, Ag, Zn and Mg, once fully lithiated, exhibited zero overpotential during deposition of Li. For materials (Ag and Mg) with high solubility, the slope of the potential profile becomes flatter, before the onset of Li deposition, matching with the behaviour of single-phase formation of metal dissolved in Li metal. Both Al and Pt have relatively small solubility in Li metal and show small but observable overpotential for Li nucleation (5 mV for Al, 8 mV for Pt).

Materials showing no solubility (Cu, Ni, C, Sn, Si) in lithium were also tested (see Supplementary Fig. 1 for phase diagrams). As shown in Fig. 1e, all five materials show a clear overpotential for Li metal nucleation. Similar to Cu, Ni does not form an alloy compound phase with Li, showing an overpotential of ~30 mV. For C, Sn and Si, even though they have compound alloy phases with Li, overpotentials still exist. For instance, Si forms an alloy compound with a high percentage of Li. At room temperature, the $Li_{15}Si_4$ phase was previously identified[22–24]. However, the crystal structure of $Li_{15}Si_4$ still differs significantly from that of Li metal. Therefore, the overpotential (~13 mV) for Li nucleation could not be eliminated. The same rule is validated on both Sn and C, with overpotentials of ~16 and ~14 mV, respectively. For all these materials without solubility in Li metal, they exhibit different overpotential values, which might result from their different thermodynamic behaviours with Li metal.

Spatial control of lithium metal deposition

The discovery and understanding of the dependence of Li metal nucleation on substrate materials opens up the opportunity for spatially controlled deposition. To demonstrate this opportunity, we carried out Li deposition on patterned substrates: materials without an overpotential serving as seeds for selective Li metal deposition, which sits on materials substrate with an overpotential (Fig. 2a). As an example, we used a copper substrate patterned with 2 μm wide Au strips for Li deposition. The gaps between Au strips were designed to vary from 1 μm to 16 μm. After galvanostatic deposition (0.1 mAh cm^{-2} at 0.5 mA cm^{-2}), it was found that Li was deposited only onto Au strips, but not on the bare Cu surface (Fig. 2b,c). It is indeed remarkable to see that there was no Li deposition even for the case with 16 μm separation between the two Au strips (Fig. 2b), implying that selective deposition of Li metal can be satisfactorily achieved even under conditions where the coverage of seeding materials is low.

We further studied the spatial control of Li metal deposition with a variety of patterns, materials and length scales (Fig. 2d–i). Colloidal Au nanoparticles (NPs) were dispersed onto a Cu substrate, leading to the deposition of Li metal preferably on Au NPs (Fig. 2d). Hexagonal arrays of metal triangles were thereafter prepared through a colloidal lithography method[25]. The SEM image in Fig. 2e shows an example of an as-prepared Au triangles array on conducting glassy carbon, followed by Li metal deposition selectively on Au triangles rather than carbon (Fig. 2f). Au triangles on a Cu substrate and Ag triangles on a glassy carbon substrate all show preferred deposition of Li metal onto the materials without nucleation barriers (Au and Ag in Fig. 2g,h). To eliminate the contribution of the surface morphology factor on the selective deposition, we also prepared a copper pattern on a glassy carbon substrate, both of which have a Li nucleation overpotential. Compared with the high density of small Li nucleation grains formed in the previous cases, only a few large Li dendrites were found on the Cu/C substrate, without any spatial selectivity (Fig. 2i).

Synthesis of nanocapsules for lithium metal

Our discovery of highly preferential nucleation of Li metal at the location of metal 'seeds' can be applied to greatly reduce the probability of dendritic growth. The essential idea is to use the Au nanoseeds to selectively nucleate and grow Li metal inside carbon nanoshells during electrochemical deposition, as shown in Fig. 3a. We have previously shown that amorphous carbon shells can transport both electrons and Li^+ ions[26]. Because amorphous carbon has an ~14 mV nucleation overpotential, our conjecture was that the nucleation of Li metal due to nano-encapsulated seeds inside the carbon nanoshells presents less of a thermodynamic barrier than nucleation of Li on the exterior of the nanocapsules.

The synthesis of the seeded nanoshells is shown in Fig. 3b (ref. 27). After modifying silica NPs (600–800 nm diameter) with 3-aminopropyltriethoxysilane, citrate-stabilized Au NPs (10–20 nm) were immobilized onto the silica surface. Thereafter, resorcinol formaldehyde (RF) resin was conformally coated onto the SiO_2@Au NP beads, followed by calcination into amorphous carbon[28,29]. The porous nature of amorphous carbon allowed removal of the silica template through HF or KOH etching, resulting in hollow carbon shells with Au NPs inside. The prepared nanocapsules are primarily composed of Au and amorphous carbon (X-ray diffraction (XRD), Supplementary Fig. 2). Thermal gravimetric analysis (TGA) indicates the mass percentage of Au is below 25% (Supplementary Fig. 3), occupying very little space owing to its large atomic mass. Scanning electron microscope (SEM) images (Fig. 3d) confirm the hollow nature of carbon spheres, with bright Au NPs clearly seen inside. A large void space was left inside for Li storage, as designed.

The structure of the nanocapsules was further characterized by transmission electron microscope (TEM). As shown in Fig. 3e, the Au NPs distributed inside the hollow carbon sphere without aggregation appear as dark spots. The carbon shell is ~20 nm thick and sufficiently robust to support the hollow architecture even with a diameter approaching 1 μm. We find that the 20 ± 5 Au NPs in the interior of the nanocapsules provide an adequate number of nucleation sites for Li metal. At higher magnifications, we clearly observe that Au NPs were anchored well onto the inner wall of the carbon shells (Fig. 3f), maintaining good electronic and ionic connection with carbon. Lattice fringes of Au NP were resolved in the high-resolution TEM image in Fig. 3g. Meanwhile, small layered graphitic grains with a typical size of ~5 nm were also observed in the carbon shell, confirming its amorphous nature with limited graphitization to offer some degree of electronic conductivity. Such a carbon microstructure has been shown to afford enough

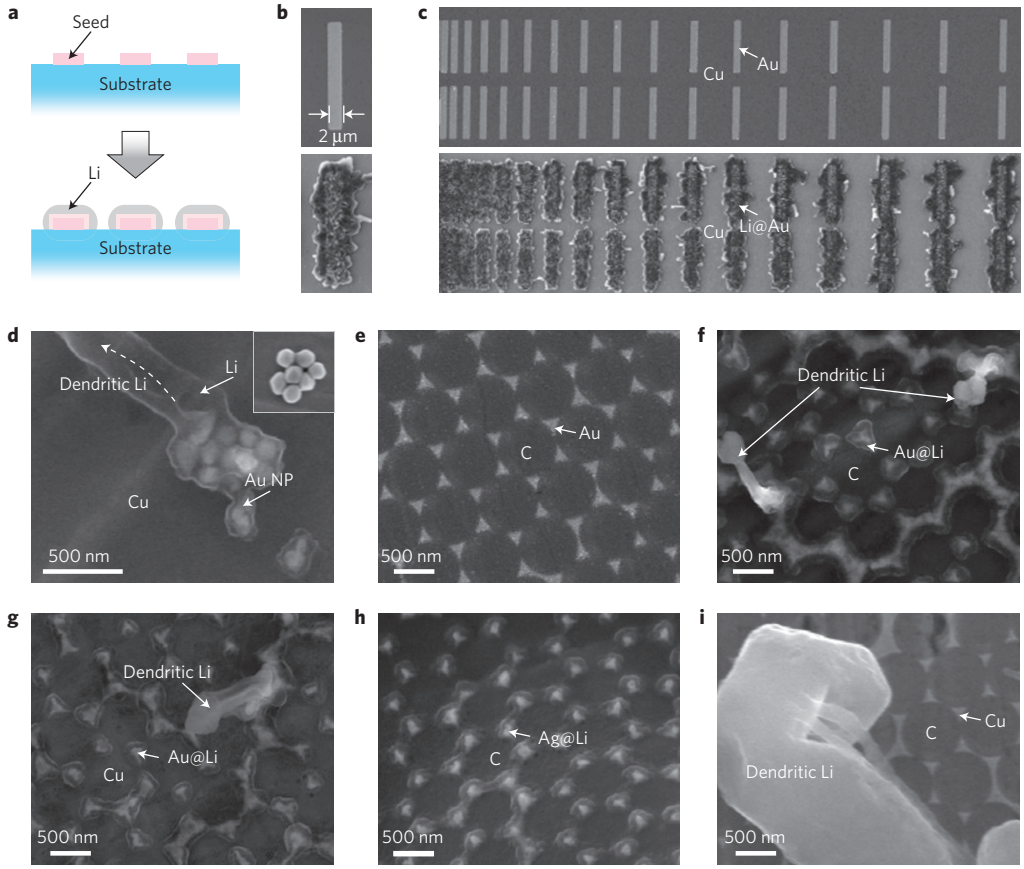

Figure 2 | Patterned deposition of Li metal. a, Schematics of patterned Li deposition. Owing to the different overpotentials during Li nucleation, Li metal would be preferably deposited on seeds without an overpotential. **b**, SEM images of a gold strip before (top) and after (bottom) Li deposition at 0.5 mA cm^{-2} for 0.1 mAh cm^{-2}. Li was found to deposit over the gold strip. The size of the gold strip is 2 μm by 16 μm. **c**, SEM images of a gold strip array with various separations before (top) and after (bottom) Li deposition. The separation increases from 1 μm (left) to 16 μm (right), where no Li metal was directly deposited into the separation. **d**, SEM images of gold NPs dispersed on copper before (inset) and after Li deposition. In addition to lithiation-induced volume expansion of gold NPs, Li metal also formed around the particles, shown as a translucent coating and dendritic shooting. **e**, SEM image of gold triangle arrays prepared by colloidal lithography on a glassy carbon (C) substrate. **f**, SEM image of Au triangle arrays on a glassy carbon substrate after Li deposition. **g**, SEM image of Au triangle arrays on a Cu substrate after Li deposition. Obvious expansion and Li coating of Au triangles is clearly shown. Dendritic Li also exists, as indicated by the arrow. **h**, SEM image of Ag triangle arrays on a glassy carbon (C) substrate after Li deposition. **i**, SEM image of Cu triangle arrays on a glassy carbon (C) substrate after Li deposition. No preferable deposition on Cu triangles was observed. Instead, large dendrites of Li formed at the expense of a high nucleation energy.

conducting channels for Li ions[24,26]. The scanning transmission electron microscope (STEM) image with clear contrast between Au and carbon (Fig. 3h) confirms the above observation. Moreover, elemental compositions of the sample were identified via electron energy loss spectroscope (EELS) mapping in Fig. 3i, confirming the structure of hollow carbon spheres with Au NPs embedded.

Stable encapsulation of lithium metal

Nanocapsules were used to fabricate a battery electrode on Cu foil via a standard slurry process (see Methods), and the cyclic voltammetry (CV) method versus Li metal reference/counter electrode was applied to study their electrochemical behaviour. Nanocapsule electrodes exhibited delithiation peaks at 240 mV, 373 mV and 495 mV, similar to pure Au film, indicating that the Au NPs inside hollow carbon shells can react with Li. Nanocapsules showed a broad background current over a wide voltage range (from 0.2 to 1.5 V), resulting from the (de)lithiation of amorphous carbon (Fig. 3c). From these results, we can infer good electric and ionic connection of Au NPs with the carbon shells.

Li metal was galvanostatically deposited from Li foil in a coin cell set-up with an appreciable areal capacity of 1 mAh cm^{-2}. For hollow carbon spheres without Au NPs, the deposition process exhibited an appreciable overpotential of 20 mV at 0.5 mA cm^{-2}, as shown in Fig. 4a. The deposited Li appeared to be outside the hollow carbon sphere, exhibiting a dendritic morphology (Fig. 4a, inset SEM image). In contrast, the nanocapsules loaded with Au NPs inside showed a much flatter potential profile without a nucleation overpotential during Li deposition at the same current density (Fig. 4b). No obvious increase of potential was observed during the prolonged deposition, which means the amorphous carbon shell is highly transparent to Li ions. The morphology is also totally different, with a smooth sphere surface free of Li metal dendrites (Fig. 4b, inset), suggesting that Li metal deposition took place inside the hollow spherical nanocapsules.

To confirm the Li metal deposition inside the hollow carbon, we examined morphological changes with *ex situ* TEM. We collected multiple pieces of evidence, suggesting metallic Li inside (Fig. 4c): no dendritic Li growth was observed with the existence of Au NPs inside the carbon shell; there are materials translucent to the electron beam inside the hollow spheres, indicating the presence of Li metal; all the Au NPs expanded after lithiation; the thickness of the shell increased from ~20 nm to 100 nm, which is consistent with the formation of a SEI layer. The porosity of amorphous carbon was eliminated because of the accumulation of a SEI, which could

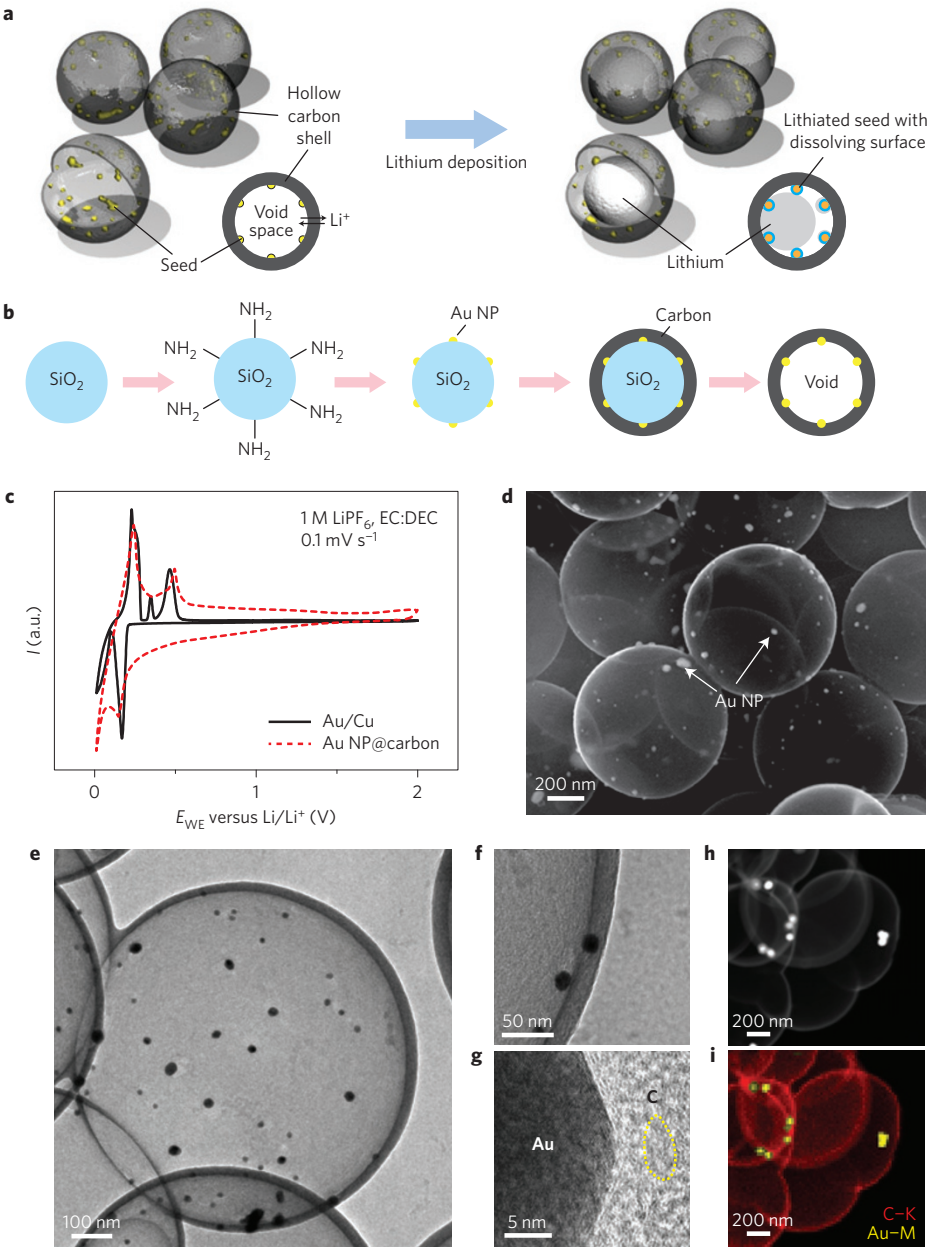

Figure 3 | Synthesis and characterization of hollow nanocapsules for Li metal. a, Schematic of Li metal nanocapsules design. Au NPs are loaded inside hollow carbon spheres, where a large void space is reserved for Li metal. Li is expected to nucleate from the Au seed. Carbon shells provide both confinement and protection of the Li metal, as well as conduction channels for both electrons and Li metal. **b**, Synthesis procedure of hollow carbon shells loaded with Au NPs inside. **c**, Cyclic voltammetry (versus Li metal electrode) study of Au film (black) and Au NPs loaded inside carbon shells (red). **d**, SEM image of hollow carbon shells. Au NPs can be seen as bright dots. **e**, TEM image of hollow carbon shells. Au NPs are visible as dark dots. **f**, TEM image magnified at the carbon shell, indicating that Au NPs are anchored on the inner surface of the carbon shell. **g**, High-resolution TEM image of Au NPs showing lattice fringes of a gold crystal. In addition, a graphitic grain with layered structure can be seen in the dashed region on the carbon side. **h**,**i**, STEM image and corresponding EELS mapping image of hollow carbon shells. Elemental information of carbon (C–K) and gold (Au–M) can be recognized through the striking signals in the mapping.

prevent direct infill of liquid electrolyte. However, it is challenging to confirm the existence of metallic Li because of its low atomic number. To further investigate the translucent material within the carbon shell, we focused the electron beam to heat up the structure. Supplementary Video 1 clearly shows that the beam-sensitive particle gradually melted into liquid with a boiling surface. Eventually, the core component of the particle is completely removed, with other structures unchanged (Fig. 4d). The melting and sublimation behaviour of the volatile property of the translucent material inside the nanocapsule is consistent with the behaviour of Li metal. In comparison, if no Au NPs were incorporated into the capsules, only dendritic Li grown outside the carbon shell was found (Fig. 4e).

To further elucidate the Li deposition process into the nanocapsules, an electrochemical dry cell was constructed for an *in situ* TEM study as in previous studies[12,24,26] (Fig. 4f). Two electrodes (Li metal and nanocapsule electrodes) are separated by natively formed Li oxide/nitride on Li metal as electrolyte. Before the experiment, no Li signal was detected in the carbon shell according to the EELS analysis (Supplementary Fig. 5). When an appropriate voltage was biased across the two electrodes, Li

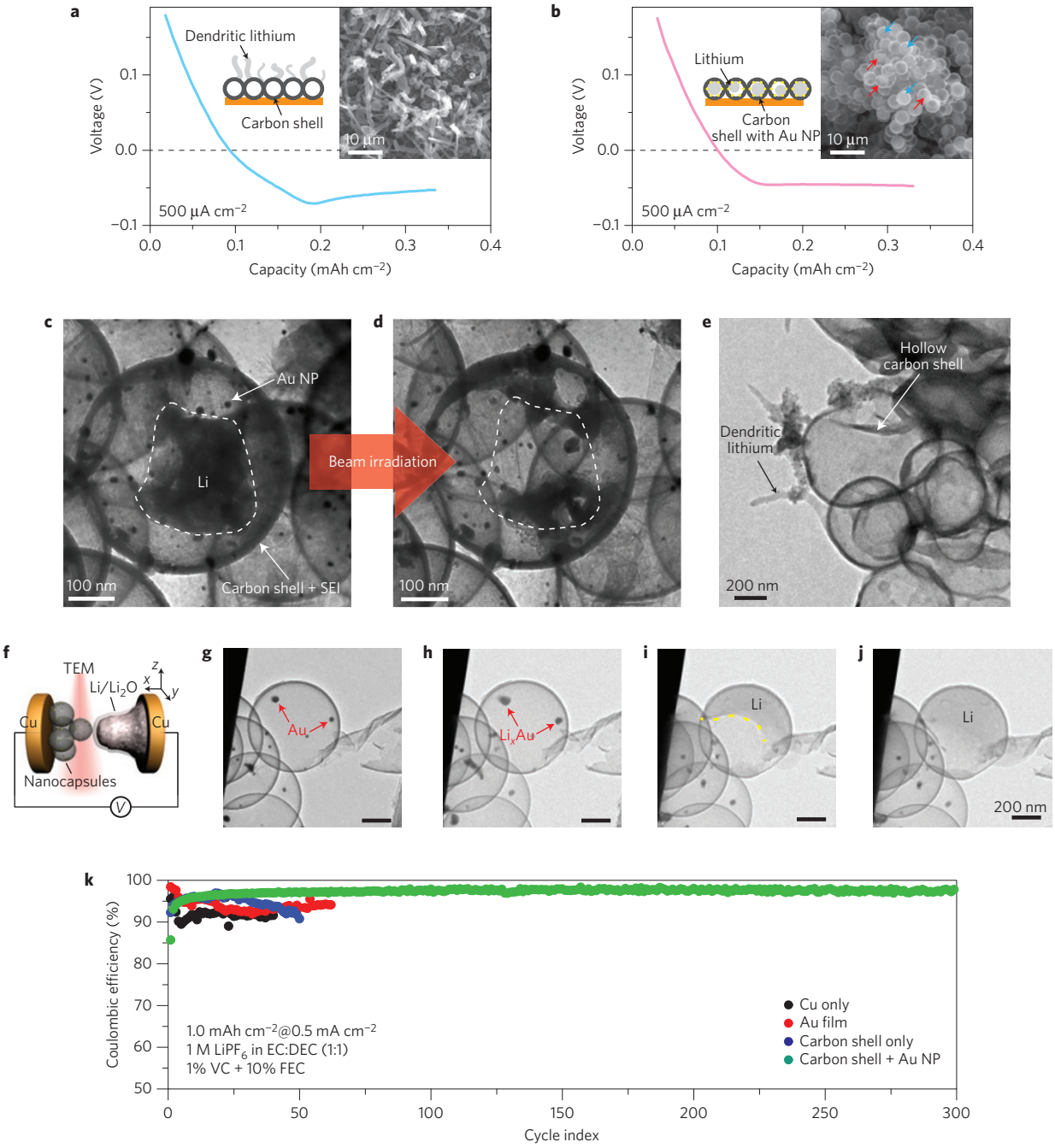

Figure 4 | Electrochemical performance of Li metal nanocapsules. a,**b**, Voltage profile during Li deposition on hollow carbon shells without (**a**) and with (**b**) Au NPs at 0.5 mA cm^{-2}. The inset shows the SEM image after deposition as well as the corresponding schematic. Fully filled and partially filled carbon spheres are marked by blue and red arrows, respectively. **c**, TEM image of nanocapsules after Li deposition. Besides the obvious Au NPs and carbon shell coated with SEI, the interior of the shell was filled with Li metal. **d**, TEM image of Li metal nanocapsules after *in situ* electron beam heating. The particle inside the shell is sublimated, with the structure unchanged. **e**, TEM image of carbon shell without Au NPs after Li deposition. Only dendritic Li metal can be observed. **f**, Schematic of dry cell for *in situ* Li deposition study with TEM. **g**–**j**, TEM snapshots of the Li deposition process inside carbon shells with Au NPs during the *in situ* Li metal plating. **k**, Coulombic efficiency of different electrodes when cycled in alkyl carbonate electrolyte.

ions started to transport towards the nanocapsules. Supplementary Video 2 shows such a filling process clearly and selected snapshots along the timeline are shown in Fig. 4g–j. At first, obvious volumetric expansion of Au NPs was observed due to lithiation of Au (ref. 30). Then, Li nucleated around the fully lithiated Au seed. As the deposition of Li continues, the Au NP gradually dissolved into the Li phase and eventually disappeared. The dissolving process is reasonable, as Au is soluble in Li and the electron beam might increase the local temperature slightly to further increase the solubility. After the deposition, two prominent peaks emerged in the EELS spectrum (Supplementary Fig. 5), which provided strong evidence for Li. We note that no Li deposition was observed outside the carbon shell until all the connected nanocapsules are fully filled, because of the additional energy needed for nucleation on the outer carbon surface. The Li filling process is reversible, as demonstrated in the Supplementary Video 3. When Li was stripped out of the nanocapsules, the Au NPs again precipitated onto the inner wall of carbon spheres in a different shape.

Such nano-encapsulation of Li metal inside hollow carbon shells can offer improved stability of Li metal electrochemical cycling with reduced side chemical reaction, because the direct contact between Li metal with electrolyte is significantly reduced. The nanocapsules loaded with Au NPs exhibited a coulombic efficiency as high as 98% in alkyl carbonate electrolyte, with stable cycling for >300 cycles. Considering the highly corrosive nature and weak SEI of alkyl carbonate electrolyte to Li metal, such a coulombic efficiency is respectable. As shown in Fig. 4k, the coulombic efficiency of bare copper substrate is low (~90%), caused by the increased surface area of dendritic Li in direct contact with electrolyte. The substrate with gold film exhibited limited improvement over copper, with a coulombic efficiency around 93%. For the hollow carbon shells without Au NPs, Li metal dendrites still form outside in contact with electrolyte, resulting in the rapid decay of coulombic efficiency to below 90% in 50 cycles. Comparatively, the nanocapsules with Au NPs exhibited stable cycling enabled by the encapsulation of Li metal, although the efficiency is not yet perfect, possibly due to the loose contact between individual shells and cracking of some shells during fabrication.

Conclusions

We discovered the substrate-dependent Li metal nucleation during its electrochemical plating. No overpotential was needed to nucleate Li metal on Au, Ag, Zn, or Mg. This can be explained by the definite solubility of the substrate in Li metal, which leads to a solid solution buffer layer before the formation of Li metal. The principle of Li metal nucleation has guided us to design hollow nanocapsules for Li metal anodes, which have no Li metal dendrites and improve the stability in corrosive carbonate electrolyte.

Methods

Preparation of thin films. Copper foil (25 μm, 99.8% metal basis, Alfa) was rinsed with 1% nitric acid (HNO_3) to remove surface coatings and oxides before serving as substrates for all the experiments. Thin films of Au, Ag, Zn, Ni, Mg, Al, Pt and Sn with a thickness of 50 nm were directly deposited onto copper foil by thermal or e-beam deposition. Si film, with a thickness of 80 nm was prepared by sputtering. Amorphous carbon film was prepared with a carbon coater (EMS150R ES), with a typical thickness of 20 nm. We found the thickness does not greatly affect the deposition behaviour of lithium metal in experiments. Moreover, the native oxide layer on all the substrates could be reduced by lithium before actual deposition at a much higher potential (usually >1 V versus Li/Li^+), leading to no difference in electrochemical results.

Preparation of patterned gold strips. For the pattered gold strips, glass slides were first coated with 100 nm of copper film to serve as flat substrate. Through a standard electron beam lithography procedure, Au/Ti film (50 nm/2 nm) was evaporated, and lifted off thereafter, before lithium deposition. The Ti adhesive layer is not expected to affect the result, considering the absence of an alloy phase between lithium and titanium[31].

Preparation of metal triangle patterns. Monodispersed silica spheres (synthesized according to the procedure below without further treatment) with a typical diameter of ~550 nm were dispersed into n-butanol (Aldrich)[32], before drop wise dripping onto a water surface in a Petri dish. A close-packed monolayer of self-assembled silica spheres was formed after adding a droplet of cetyl trimethylammonium bromide solution (CTAB, Aldrich, 10 mM). Acid-treated copper foils were used to pick the monolayer up as a hexagonal template for evaporation of metals with a thickness of 20 nm. After removal of the silica template through sonication, the substrate was directly used for electrochemical deposition at a current density of 0.5 mA cm^{-2} for 10 min. A lithium iron phosphate electrode was used as the Li source here for better uniformity.

Preparation of amino group functionalized silica spheres. A typical synthesis started from silica spheres, which were produced according to a modified Stöber method[33], from hydrolysis of 8 ml tetraethyl orthosilicate (TEOS, Aldrich) in a mixture of 80 ml isopropanol alcohol (IPA, Fisher Scientific) and 12 ml water. Under vigorous stirring, 8 ml of concentrated ammonium hydroxide ($NH_3 H_2O$, EMD Millipore) was added into the solution. The reaction was left at room temperature for two hours until all the TEOS decomposed into silica spheres. After centrifuging three times and washing with IPA/water/water, all the particles were dispersed in 100 ml IPA by sonication. The solution was stirred at 60 °C overnight after 1 ml (3-aminopropyl)triethoxysilane (APTES, Aldrich) was added. After centrifuging three times and washing with IPA/water/water, the silica spheres were dispersed in 20 ml water by sonication.

Preparation of gold nanoparticles. To prepare gold nanoparticles (NPs), a classic recipe was used[34]. Typically, 1 ml sodium citrate solution (Alfa, 10%) was diluted in 100 ml water. After heating the solution to boiling, 200 μl chloroauric acid ($HAuCl_4$, Aldrich, 0.5 M) was quickly injected. The reaction was allowed for 5 min before cooling the solution to room temperature. The as-prepared gold NPs exhibited an average diameter of ~20 nm.

Adsorption of gold NPs onto silica spheres. The 100 ml gold NP colloidal suspension was added into the silica suspension in five equal batches, rendering the spheres from white to pink and finally purple. After each mixing, the spheres were separated by centrifuging. No wash was necessary except for the last batch.

Coating spheres with amorphous carbon. All the particles were dispersed in 240 ml water with gentle sonication for coating of formaldehyde resin (RF; refs 28,29). Care must be taken to reduce the desorption of gold NPs. 8 ml cetyl trimethylammonium bromide (CTAB, Aldrich, 10 mM) and 0.8 ml concentrated ammonium hydroxide was then added, followed by stirring for 10 min, until the surface charge of all the particles was completely altered by CTAB. Thereafter, 300 mg resorcinol (Aldrich) and 420 μl formaldehyde solution (Aldrich, 37% wt% in water) were added and stirred for 8 h. The thickness of the resin coating could be easily tuned by simultaneously changing the amount of resorcinol and formaldehyde. After centrifuging three times and washing with water/water/ethanol, the particles were collected for calcination. A typical calcination procedure includes heating to 600 °C at 1 °C min^{-1} and then to 900 °C at 10 °C min^{-1}. The sample was kept at 900 °C to carbonize all the resin shells.

Removal of silica template. To create the space for lithium metal storage, silica templates could be easily removed through either potassium hydroxide (KOH, J.K. Baker, 5M) or hydroflouride (HF, Aldrich, 10%) etching. Although the HF etching took only half an hour at room temperature to remove all the silica, the KOH etching that takes up to 48 h at 70 °C under reflux is preferred for safety concerns. 10% IPA was always incorporated to improve the wetting. After the etching process, the sample was filtered and washed through vacuum filtration. The solid product was collected and dried in a vacuum oven at 80 °C for 24 h before use.

Preparation of electrodes with nanocapsules. Nanocapsules with gold, carbon black (Super P, TIMCAL) and polyvinylidene difluoride binder (PVDF, Kynar, HSV900) were mixed with a mass ratio of 1:1:1, taking into consideration the extremely low density of hollow nanocapsules. The nanocapsules with this ratio took approximately the same volume ratio as our previous silicon pomegranate structure[26] with a mass ratio of 8:1:1. The mixture was stirred in *N*-methylpyrrolidone overnight (NMP, Aldrich) to form a slurry with a typical ratio of 0.1 g ml^{-1} (nanocapsules/NMP). After casting the slurry onto a copper foil with a doctor blade with designated thickness (typically 250 μm gauge for a final thickness of ~10 μm), the electrode was dried in vacuum oven overnight. A control sample without gold NPs loaded was prepared according to the same procedure. Calendaring was avoided here to prevent damage to the hollow structure.

General characterizations. Standard characterization techniques for nanotechnology were used to retrieve basic information related to the nanocapsules, including X-ray diffraction (PANalytical X'Pert, Ni-filtered Cu Kα radiation), scanning electron microscopy (FEI Sirion), and (scanning) transmission electron microscopy (FEI Tecnai G2 F20 X-twin and FEI Titan). All *ex situ* studies with SEM and TEM were done after disassembling the tested electrodes in an argon glovebox and thoroughly washing with dimethyl carbonate (DMC, Aldrich).

Mass percentage determination. The mass percentage of gold in the hollow nanocapsules was determined through the weight loss curves measured under stimulated air atmosphere (20% oxygen + 80% argon, Airgas, 5N) on a TG/DTA system (Netzsch STA 449) with a heating rate of 5 °C min^{-1}. Hollow carbon shells without gold particles served as the control sample with the identical heating conditions for error correction.

***In situ* transmission electron microscope characterization.** A specialized dual-probe transmission electron microscope holder (Nanofactory Instruments, AB) capable of electrical bias and piezoelectric manipulation was used for the *in situ* studies. The nanocapsules were loaded onto a static copper wire (working electrode) by drop-casting, while a movable tungsten wire (counter and reference electrode) was loaded with a tiny amount of lithium. The surface of lithium was naturally oxidized, which leads to a ~100 nm lithium oxide/nitride layer to serve

as solid electrolyte with huge resistance. After positioning the lithium piece onto a single nanocapsule, the copper wire was biased to −3.0 V versus the tungsten wire, allowing lithium ions to flow to the nanocapsule. By reversing the bias, lithium metal could be stripped out from the nanocapsule. During the testing, the resistance of the system varies depending the state of lithium deposition. Therefore, a constant rate could hardly be maintained throughout the lithium metal plating/stripping process.

Electrochemical deposition of lithium metal on planar surface. For the planar deposition of lithium metal, pouch cells with three terminals were used. The $LiFePO_4$ electrode (~2 mAh cm^{-2}, MTI) was precharged to 50% before being embedded between two separators (Celguard, 25 μm), serving as the reference electrode (RE) with stable potential. The working electrode (WE) with a thin film coating and the counter electrode (CE) with lithium foil (750 μm, Alfa) were assembled on each side of the separator. The area was defined by the size of lithium foil. Excess electrolyte (1M LiPF6 in EC/DEC, Selectilyte, BASF) was injected to completely wet the separator and electrodes before the pouch cell was sealed. The galvanostatic deposition of lithium was carried out on a potentiostat (VMP-300, Bio-logic) with varying current densities (from 10 μA cm^{-2} to 100 μA cm^{-2}). Despite the intrinsic capacity of the film, if any, the deposition continued until the potential became stable ($\Delta V < 0.01$ V in 30 min) or more than 0.2 mAh cm^{-2} capacity of lithium metal was applied, whichever was later.

Cycling performance tests. Assembled inside an Ar-filled glovebox (MBraun, O_2 and H_2O <1.0 ppm), coin-type cells (2032) were used for all cycling performance tests. A piece of prepared electrode (1 cm^2), double layers of polyethylene separator (Celgard 2250) and a piece of lithium foil (1 cm^2 × 750 μm, Alfa) were closely stacked into the coin cell enclosure, augmented with 200 μl electrolyte (1.0 M LiPF6 in EC/DEC (Selectilyte, BASF), with 1% vinyl carbonate (VC, Novolyte Technologies) and 10% fluoroethylene carbonate additive). The cells were cycled galvanostatically on an ARBIN system. A typical test programme for pure nanocapsules started with 10 activation cycles between 0.01 V and 1 V versus Li/Li^+, followed by a cycling programme including: Step 1, lithiation of the electrode to 0 V versus Li/Li^+; Step 2, deposition of the desired amount of lithium metal; and Step 3, stripping out all lithium ions to 1.0 V. The coulombic efficiency was calculated as $Q_{delithiation}/Q_{lithiation+deposition} \times 100\%$, where $Q_{delithiation}$ and $Q_{lithiation+deposition}$ refer to the capacities involved in step 3 and steps 1 + 2, respectively.

Received 28 October 2015; accepted 22 January 2016; published 22 February 2016

References

1. Tarascon, J. M. & Armand, M. Issues and challenges facing rechargeable lithium batteries. *Nature* **414**, 359–367 (2001).
2. Chu, S. & Majumdar, A. Opportunities and challenges for a sustainable energy future. *Nature* **488**, 294–303 (2012).
3. Whittingham, M. S. History, evolution, and future status of energy storage. *Proc. IEEE* **100**, 1518–1534 (2012).
4. Bruce, P. G., Freunberger, S. A., Hardwick, L. J. & Tarascon, J.-M. $Li–O_2$ and Li–S batteries with high energy storage. *Nature Mater.* **11**, 19–29 (2012).
5. Xu, W. *et al.* Lithium metal anodes for rechargeable batteries. *Energy Environ. Sci.* **7**, 513–537 (2014).
6. Whittingham, M. S. Electrical energy storage and intercalation chemistry. *Science* **192**, 1126–1127 (1976).
7. Aurbach, D., Zinigrad, E., Cohen, Y. & Teller, H. A short review of failure mechanisms of lithium metal and lithiated graphite anodes in liquid electrolyte solutions. *Solid State Ion.* **148**, 405–416 (2002).
8. Kamaya, N. *et al.* A lithium superionic conductor. *Nature Mater.* **10**, 682–686 (2011).
9. Bouchet, R. *et al.* Single-ion BAB triblock copolymers as highly efficient electrolytes for lithium-metal batteries. *Nature Mater.* **12**, 452–457 (2013).
10. Ding, F. *et al.* Dendrite-free lithium deposition via self-healing electrostatic shield mechanism. *J. Am. Chem. Soc.* **135**, 4450–4456 (2013).
11. Qian, J. *et al.* High rate and stable cycling of lithium metal anode. *Nature Commun.* **6**, 6362 (2015).
12. Zheng, G. *et al.* Interconnected hollow carbon nanospheres for stable lithium metal anodes. *Nature Nanotech.* **9**, 618–623 (2014).
13. Yan, K. *et al.* Ultrathin two-dimensional atomic crystals as stable interfacial layer for improvement of lithium metal anode. *Nano Lett.* **14**, 6016–6022 (2014).
14. Bhattacharyya, R. *et al. In situ* NMR observation of the formation of metallic lithium microstructures in lithium batteries. *Nature Mater.* **9**, 504–510 (2010).
15. Chandrashekar, S. *et al.* ^{7}Li MRI of Li batteries reveals location of microstructural lithium. *Nature Mater.* **11**, 311–315 (2012).
16. Huggins, R. *Advanced Batteries* 123–149 (Springer, 2009).
17. Aurbach, D., Weissman, I., Schechter, A. & Cohen, H. X-ray photoelectron spectroscopy studies of lithium surfaces prepared in several important electrolyte solutions. A comparison with previous studies by Fourier transform infrared spectroscopy. *Langmuir* **12**, 3991–4007 (1996).
18. López, C. M., Vaughey, J. T. & Dees, D. W. Morphological transitions on lithium metal anodes. *J. Electrochem. Soc.* **156**, A726 (2009).
19. Aurbach, D. Review of selected electrode–solution interactions which determine the performance of Li and Li ion batteries. *J. Power Sources* **89**, 206–218 (2000).
20. Visco, S., Nimon, Y. & Katz, B. Compositions and methods for protection of active metal anodes and polymer electrolytes. US patent 20040131944 A1 (2004).
21. La Mantia, F., Wessells, C. D., Deshazer, H. D. & Cui, Y. Reliable reference electrodes for lithium-ion batteries. *Electrochem. Commun.* **31**, 141–144 (2013).
22. Obrovac, M. N. & Christensen, L. Structural changes in silicon anodes during lithium insertion/extraction. *Electrochem. Solid-State Lett.* **7**, A93 (2004).
23. McDowell, M. T., Lee, S. W., Nix, W. D. & Cui, Y. 25th anniversary article: understanding the lithiation of silicon and other alloying anodes for lithium-ion batteries. *Adv. Mater.* **25**, 4966–4985 (2013).
24. McDowell, M. T. *et al. In situ* TEM of two-phase lithiation of amorphous silicon nanospheres. *Nano Lett.* **13**, 758–764 (2013).
25. Hulteen, J. C. *et al.* Nanosphere lithography: size-tunable silver nanoparticle and surface cluster arrays. *J. Phys. Chem. B* **103**, 3854–3863 (1999).
26. Liu, N. *et al.* A pomegranate-inspired nanoscale design for large-volume-change lithium battery anodes. *Nature Nanotech.* **9**, 187–192 (2014).
27. Liu, Y., Goebl, J. & Yin, Y. Templated synthesis of nanostructured materials. *Chem. Soc. Rev.* **42**, 2610–2653 (2013).
28. Li, N. *et al.* Sol-gel coating of inorganic nanostructures with resorcinol-formaldehyde resin. *Chem. Commun.* **49**, 5135–5137 (2013).
29. Liu, J. *et al.* Extension of the Stöber method to the preparation of monodisperse resorcinol-formaldehyde resin polymer and carbon spheres. *Angew. Chem. Int. Ed. Engl.* **50**, 5947–5951 (2011).
30. Zeng, Z., Liang, W.-I., Chu, Y.-H. & Zheng, H. *In situ* TEM study of the Li–Au reaction in an electrochemical liquid cell. *Faraday Discuss.* **176**, 95–107 (2014).
31. Massalski, T. B. & Okamoto, H. *Binary Alloy Phase Diagrams* (ASM International, 1990).
32. Moon, G. D. *et al.* Assembled monolayers of hydrophilic particles on water surfaces. *ACS Nano* **5**, 8600–8612 (2011).
33. Stöber, W., Fink, A. & Bohn, E. Controlled growth of monodisperse silica spheres in the micron size range. *J. Colloid Interface Sci.* **26**, 62–69 (1968).
34. Frens, G. Controlled nucleation for the regulation of the particle size in monodisperse gold suspensions. *Nature* **241**, 20–22 (1973).

Acknowledgements

This work was supported by the Assistant Secretary for Energy Efficiency and Renewable Energy, Battery Materials Research (BMR) Program in the Office of Vehicle Technologies of the US Department of Energy. H.-W.L. was supported by Basic Science Research Program through the National Research Foundation of Korea under Contract No. NRF-2012R1A6A3A03038593.

Author contributions

K.Y. and Y.C. conceived the idea. K.Y., F.X. and P.-C.H. conducted the film deposition. K.Y. and Z.L. synthesized hollow spheres. K.Y. carried out the electrochemical tests. H.-W.L., Y.L. and Z.L. performed TEM characterizations. K.Y., P.-C.H., J.Z. and Z.L. worked on other characterizations. Y.C. and S.C. supervised the project and participated in the planning of research. K.Y., S.C. and Y.C. co-wrote the paper. All authors discussed the results and commented on the manuscript.

Additional information

Supplementary information is available online. Reprints and permissions information is available online at www.nature.com/reprints. Correspondence and requests for materials should be addressed to Y.C.

Competing interests

The authors declare no competing financial interests.